Research Square

Preprints are preliminary reports that have not undergone peer review.
They should not be considered conclusive, used to inform clinical practice,
or referenced by the media as validated information.

Comparative Thermal Stability of Perovskite Solar Cells Using DFT and OghmaNano

Darko A. Noori

darko.noori@univsul.edu.iq

University of Sulaimani

Eman Qabil Majeed

University of Sulaimani

Research Article

Keywords: Perovskite solar cells, Ba0.75Ca0.25TiO3, Ba2CeBiO6, Rb2YCuI6, Thermal stability, Density Functional Theory, OghmaNano simulation

Posted Date: November 10th, 2026

DOI: https://doi.org/10.21203/rs.3.rs-11336175/v1

License: This work is licensed under a Creative Commons Attribution 4.0 International License.
Read Full License

Additional Declarations: No competing interests reported.

Comparative Thermal Stability of Perovskite Solar Cells Using DFT and OghmaNano

Darko A. Noori*[1] Eman Qabil Majeed[1]

October 14, 2026

[1]University of Sulaimani, College of Science, Department of Physics, Sulaymaniyah, 46001, Kurdistan Region, Iraq

*Corresponding author: darko.noori@univsul.edu.iq

Abstract

Perovskite solar cells have become excellent photovoltaic devices because of their extraordinary optoelectronic properties. However, their practical use is limited by their low thermal stability. This research focuses on the photovoltaic properties and thermal stability of three inorganic perovskite materials: $\mathrm{Ba_{0.75}Ca_{0.25}TiO_3}$, $\mathrm{Ba_2CeBiO_6}$, and $\mathrm{Rb_2YCuI_6}$. To predict device performance, the density functional theory (DFT) method was first applied to determine the optical and electronic properties of the perovskite structures, which were then used as inputs for the OghmaNano simulator. The study initially considered simple FTO/Perovskite/Au single-active-layer cells without transport layers over the temperature range of 300–325 K. The $\mathrm{Ba_{0.75}Ca_{0.25}TiO_3}$ material showed the highest thermal stability, with the lowest PCE loss of about 3%, compared with 6% for $\mathrm{Ba_2CeBiO_6}$ and 7.5% for $\mathrm{Rb_2YCuI_6}$. Subsequently, FTO/Perovskite/Perovskite/Au bilayer devices were studied using perovskite–perovskite interface engineering over the temperature range of 300–330 K. As the temperature increased, the open-circuit voltage decreased, while the short-circuit current density remained almost constant, resulting in a relatively modest reduction in PCE. Charge carrier generation, charge carrier recombination, charge carrier density, quantum efficiency, and thermal stability were investigated for the bi-active-layer devices $FTO/Ba_2CeBiO_6/Rb_2YCuI_6/Au$ and $FTO/Rb_2YCuI_6/Ba_{0.75}Ca_{0.25}TiO_3/Au$, without electron and hole transport layers, respectively. Combining DFT results, interface engineering, and OghmaNano device simulations provides a powerful approach for designing simple, effective, and highly thermally stable perovskite solar cells.

Keywords: Perovskite solar cells, $\mathrm{Ba_{0.75}Ca_{0.25}TiO_3}$, $\mathrm{Ba_2CeBiO_6}$, $\mathrm{Rb_2YCuI_6}$, Thermal stability, Density Functional Theory, OghmaNano simulation.

1 Introduction

The history of semiconductors and photovoltaics goes back more than 150 years. Edmond Becquerel first discovered the photovoltaic effect in 1839, when he observed a photoelectric current flowing between silver electrodes immersed in an electrolyte solution [1]. Since then, photovoltaic technology has gone through three generations, with the first generation being crystalline-silicon cells, which remain the most advanced and proven technology [2]. Then, the second generation of thin-film cells was created to decrease the amount of materials used and production costs, and increase flexibility [3, 4]. The third generation of solar cells, such as perovskite, organic, dye-sensitized, and quantum dot solar cells, has been created to improve earlier technologies [5], [6]. But stability and toxicity still pose problems [7].

Perovskite materials have a crystal structure ABX_3, with **A** and **B** being cations of different sizes and **X** being an anion like oxygen or halides [8]. Based on X, they are categorized as either oxide or halide perovskites. Their flexible structure makes their properties optically, electrically, and magnetically versatile for uses such as photovoltaics, fuel cells, light-emission devices, and catalysis. The structure of perovskites can be determined by: $t = \frac{R_A+R_X}{\sqrt{2}(R_B+R_X)}$, where R_A, R_B, and R_X represent the ionic radii of the A-site cation, B-site cation, and X-site anion, respectively [9]. In general, a tolerance factor between 0.9 and 1 indicates a stable cubic structure, whereas lower tolerance factors may give rise to distorted structures [10]. In addition, perovskite absorbers have very high absorption coefficients of (10^4 to 10^5 cm^{-1}), and bandgap tuning is possible by manipulating either A, B, or X ions [11, 12]. Also Stranks and co-workers observed that $CH_3NH_3PbI_{3-x}Cl_x$ has electron and hole diffusion lengths larger than 1μm [13]. Although highly efficient, Perovskite solar cells (PSCs) are highly unstable due to the reasons like instability in nature, humidity, oxygen, temperature, and exposure to light [14, 15]. Humidity speeds up the degradation of perovskites due to hydrolysis reactions and must be kept below 1% [16, 17]. Walsh et al. suggested an acid-base reaction mechanism for moisture degradation of $(MAPbI_3)$ [18]. Also, thermal annealing is needed to eliminate solvent residues and crystallize the perovskite [19], whereas high temperatures lead to the decomposition of organic perovskites into PbI_2, CH_3NH_2, and HI [20].

Metal halide perovskites have come to prominence in photovoltaics after the emergence of solid-state perovskite solar cells with efficiencies of 9.7% in 2012 [21].In PSCs, the perovskite material is sandwiched between the electron-transporting layer and the hole-transporting layer. When illuminated, electron-hole pairs are formed, which are transported by the ETL and the HTL, respectively, and the electrodes collect this current. Since these materials have very good light-absorption properties, very thin absorber layers are possible in PSCs. Perovskite oxides usually follow the structure ABO_3, in which the A site is an alkaline earth or rare earth and the B site is a transition metal bonded to oxygen [22, 23]. Ferroelectric properties exist in materials like $BaTiO_3$, whereas oxide perovskites $Ba_2YCu_3O_7$ can be superconducting and magnetic in nature; such characteristics make them potential candidates for energy-related applications like solid oxide fuel cells, batteries, and thermal energy storage [22, 24]. Two-dimensional (2D) perovskites are made up of metal halide octahedral layers interspaced with bulky organic spacer cations. As opposed to 3D perovskites, the 2D architecture makes them more environmentally stable and

optoelectronically tunable, hence appealing for solar cells and photodetectors, among others [25]. The conventional metal-halide perovskites 3D perovskites typically have $\mathrm{ABX_3}$ formula, where A= MA^+, FA^+, or Cs^+, B=Pb^{2+} or Sn^{2+}, while X is anions like I^-, Br^-, or Cl^-[26]. They have high absorption coefficients, bandgap tunability, low exciton binding energies, high carrier mobility, and long carrier diffusion lengths [27–30]. However, the sensitivity to moisture, oxygen, heat, and light, as well as ion movement, reduces stability and makes encapsulation necessary [28, 31].

The double perovskites have the chemical formula $\mathrm{A_2BB'X_6}$ and comprise two different B-site ions, allowing for more structural variation [32]. These materials typically offer better thermal stability and electronically tunable properties. Halide double perovskites (HDPs), with the structure $\mathrm{A_2B'B''X_6}$, where A=Cs, B'=Ag, Na, Cu, Au, B''=Bi, In, and X=Br, Cl, or I, have been examined as lead-free substitutes owing to their promising optoelectronic features and low toxicity [33, 34]. Similarly, the Oxide double perovskites (ODPs) with their chemical formula$\mathrm{A_2B'B''O_6}$ also exhibit structural stability, tunable band gaps, and potential as visible light-driven photocatalysts [35]. Double perovskite structures can be predicted by calculating their tolerance factors and octahedral factors (μ), where stable structures will exist for t = 0.81-1.11 and μ = 0.44-0.90 [36]. But Perovskite single structures need $0.414 < \mu < 0.732$ to have stable BX6 octahedra [37]. Many double perovskites like Cs2AgBiX6 have indirect bandgaps, and this hinders their photovoltaic performance [38]. Direct band gap behavior is also observed in other materials, such as Cs2AgInCl6 and ordered vacancy double perovskites [39, 40]. The Ag-Bi family of double perovskites also exhibits a relatively broad bandgap, but it boasts a long carrier lifetime, small effective mass, and thermal/photochemical stability [41].

Based on the literature reviewed, three lead-free perovskite materials, $\mathrm{Ba_{0.75}Ca_{0.25}TiO_3}$ as Ca doped Perovskite material, $\mathrm{Ba_2CeBiO_6}$ as double oxide perovskite material, and $\mathrm{Rb_2YCuI_6}$ as double halid perovskite materal, were considered suitable and selected for further study because the authors of the cited papers reported their structural stability and potential for photovoltaic applications. In light of these findings, a detailed analysis of these materials was carried out simultaneously using the OghmaNano simulation platform under the same device setup and operating conditions, allowing their photovoltaic properties and stability to be compared under consistent conditions. The analysis primarily focuses on the simulated photovoltaic properties, charge generation and recombination processes, photon absorption, and stability of the selected materials. In addition, the results obtained from the simulations were used to design and simulate two optimized device architectures, FTO/$\mathrm{Rb_2YCuI_6}$/$\mathrm{Ba_{0.75}Ca_{0.25}TiO_3}$/Au and FTO/$\mathrm{Ba_2CeBiO_6}$/$\mathrm{Rb_2YCuI_6}$/Au, to further investigate the photovoltaic properties and stability of these material combinations. Ultimately, this study aims to evaluate the potential of these lead-free perovskite materials for photovoltaic applications and to highlight material combinations that can provide stable and efficient perovskite solar cells.

2 Methodology

This section explains the method we have used to model and simulate perovskite solar cells using the OghmaNano simulator. The methodology mainly comprises the assessment of the photovoltaic performance of different perovskite active layers under the exact device configuration and operating conditions, without the application of an ETL or HTL. The device simulated in our case has two metal contacts: FTO (50 nm) on the front and Au (100 nm) on the back, respectively. At the same time, the thickness of each active layer has been fixed at 500 nm. We have compared $Ba_{0.75}Ca_{0.25}TiO_3$, Ba_2CeBiO_6, and Rb_2YCuI_6 under the same set of simulation parameters and operating conditions to make sure that the comparison is fair and consistent. Besides this, it also presents the simulation design, parameters, and procedures involved before and during the evaluation of the candidate materials according to a set of simulated photovoltaic performance criteria.

2.1 Design of the Study

In the present investigation, we employed $Ba_{0.75}Ca_{0.25}TiO_3$, Ba_2CeBiO_6, and Rb_2YCuI_6 as novel materials for the development of perovskite interfaces (respectively, single-perovskite Ca-doped $BaTiO_3$, double-oxide perovskite, and halide double perovskite) in combination with the active layer materials. The basic design of the device simulated in this paper is FTO/Perovskite/Au. Note that the simulation analysis was carried out on the active layer only by introducing the new perovskite materials through an interfacial engineering method, and the device did not include an electron transport layer (ETL) or a hole transport layer (HTL). Firstly, the optoelectronic properties of the newly developed perovskite materials were determined by means of DFT simulations and published articles, and afterwards, they were implemented into the simulation tool (the schematic illustration representing the method and its sequence is given below; see Figure 1). Next, the thermal stability of different active layers was investigated and compared. The cell structures FTO/Rb_2YCuI_6/$Ba_{0.75}Ca_{0.25}TiO_3$/Au and FTO/Ba_2CeBiO_6/Rb_2YCuI_6/Au were studied in terms of their efficiency, stability, charge recombination and generation, and photon absorption in these experiments.

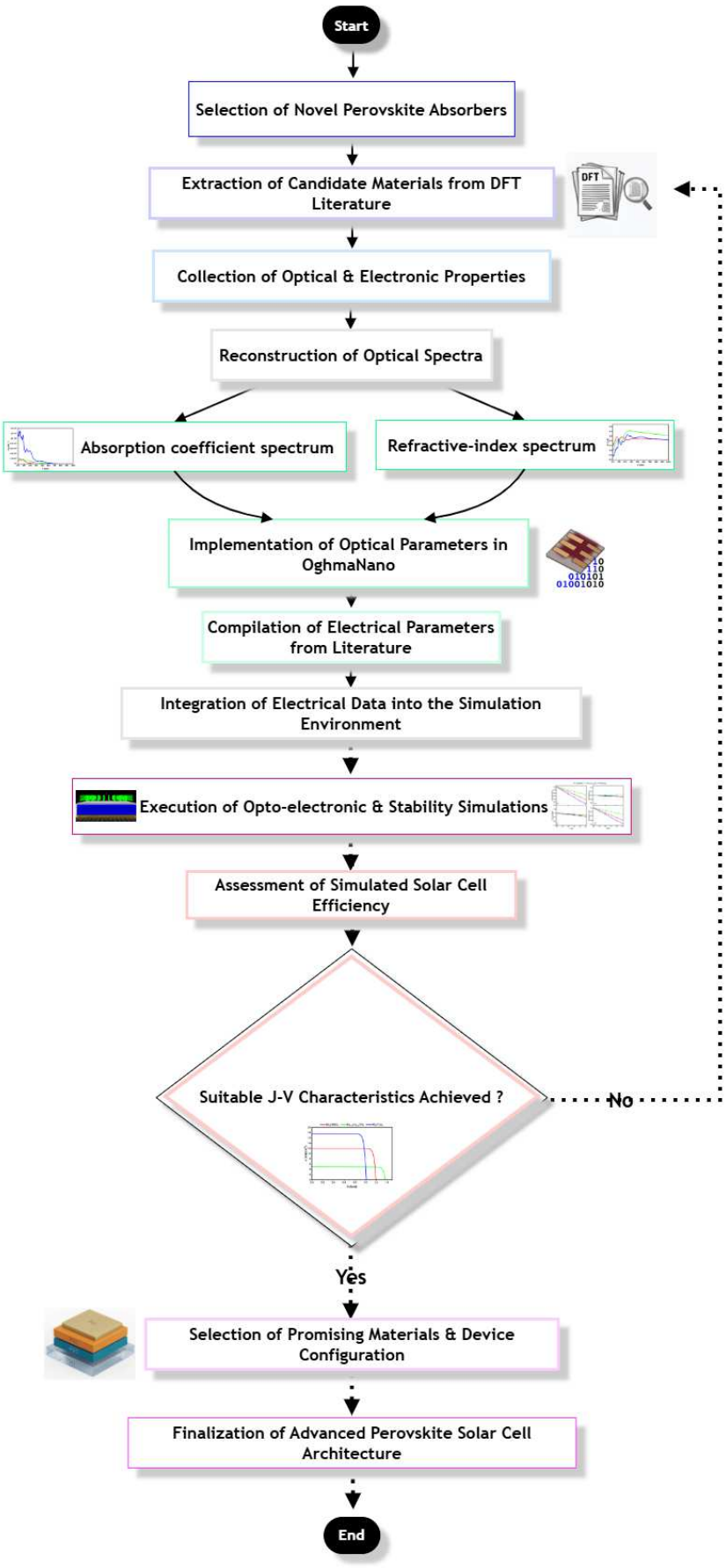


Figure 1: Flowchart illustrating the material selection process and their implementation in the OghmaNano simulator for perovskite solar cell simulations.

2.2 Simulation Parameters

The detailed parameters in this simulation, such as layer thickness, electron-hole mobilities, electron affinity, dielectric constant, and environmental conditions, are shown in the table below.

Table 1: The detailed parameters of perovskite solar cells simulation based on different perovskite structures as active layer in OghmaNano software

Parameters	$Ba_{0.75}Ca_{0.25}TiO_3$ **[42–45]**	Ba_2CeBiO_6 **[46–49]**	Rb_2YCuI_6 **[50, 51]**
Thickness (nm)	500	500	500
Electron mobility (m^2/V.s)	$1.2x10^{-4}$	$1.17x10^{-2}$	$1x10^{-2}$
Hole mobility (m^2/V.s)	$1.2x10^{-4}$	$6.5x10^{-3}$	$1.0x10^{-2}$
Effective density of electron states (m^{-3})	$6x10^{24}$	$1.0x10^{25}$	$5.0x10^{25}$
Effective density of hole states (m^{-3})	$6.0x10^{24}$	$1.0x10^{25}$	$1.0x10^{26}$
Free electron to free hole recombination rate (m^3/s)	$1.0x10^{-15}$	$1.0x10^{-15}$	$1.0x10^{-15}$
Electron affinity (eV)	3.8	3.9	4
Energy bandgap (eV)	1.775	1.75	1.67
Relative permittivity (a.u.)	11	4.4	4.5
Donor concenteration (m^{-3})	-	-	-
Acceptor concenteration (m^{-3})	-	-	-

2.3 Simulation Method

All simulation tasks were performed at 300 K, with a series resistance of 11 Ohm and a shunt resistance of $1*10^6$ Ohm under the AM1.5G standard as the incoming light source. In this regard, the data were collected from four simulation work structures. The first simulation work was designed for the single active layer without a transporting layer for each of the double perovskite materials. Then the temperature stability study were investigated from 300 K to 325 K, and the efficiency of the cells was compared. Finally the new design of perovskite solar cells are achieved with the idea of the double active layer in the cell.

The OghmaNano software is based on different standard techniques, including the bipolar drift-diffusion model of the current flux density for electrons and holes, which are given by the following equation [52–56]:

$$J_n = q\mu_c n\frac{\partial E_c}{\partial x} + qD_n\frac{\partial n}{\partial x} \tag{1}$$

$$J_p = q\mu_n p\frac{\partial E_v}{\partial x} - qD_p\frac{\partial p}{\partial x} \tag{2}$$

where

$$n = N_c \exp\left(-\frac{E_c - E_F}{k_B T}\right) \tag{3}$$

$$p = N_v \exp\left(-\frac{E_F - E_v}{k_B T}\right) \tag{4}$$

where J_n and J_p are an electron and hole flux densities, q is an elementary charge electron, n and p are a free electron and hole concentrations, μ_n and μ_p represent the electron and hole mobility, D_n and D_p indicates the electron and hole diffusion coefficient, E_c and E_v shows the free electron and hole mobility edge. Also, the equations of continuity for electrons and holes in position space are indicated as follows,

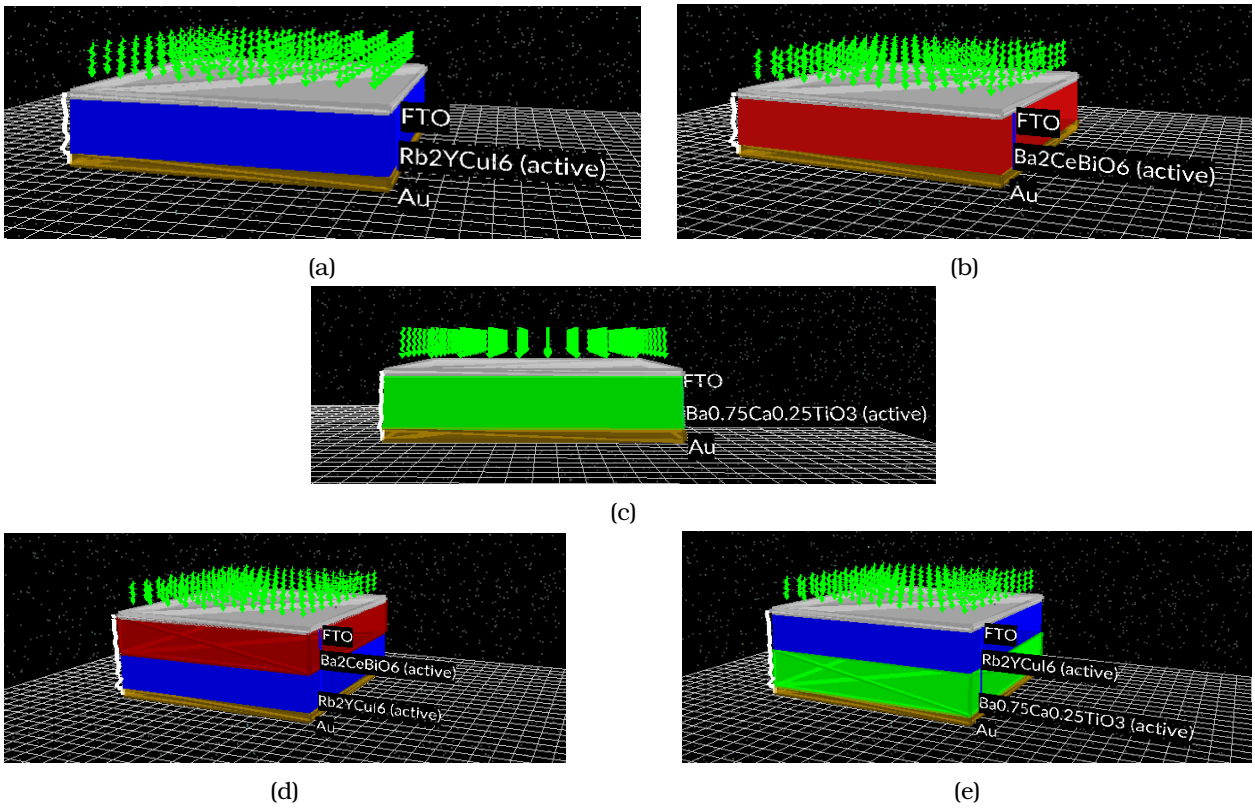


Figure 2: 3D Structure of single and double absorber layer PSCs (a),(b),(c) are single absorber layer PSCs with the general structure of FTO/absorber/Au and (d),(e) are double Absorber layer PSCs with the general structure of FTO/Double Absorber/Au, these images extracted from oghmanano simulation software.

$$\frac{\partial J_n}{\partial x} = q\left(R_n - G + \frac{\partial n}{\partial x}\right) \tag{5}$$

$$\frac{\partial J_p}{\partial x} = -q\left(R_p - G + \frac{\partial p}{\partial x}\right) \tag{6}$$

where R_n and R_p are the net recombination rate, G is the free carrier generation rate. As well as, the Poisson equation for calculating the internal electrostatic potential is given by,

$$\nabla^2\phi = -\frac{q(n-p)}{\varepsilon_0\varepsilon} \tag{7}$$

where ∇^2 is Laplacian operator, ε_0 the permittivity of the vacuum, ε is the relative permittivity, and ϕ denote the voltage profiles.

charge carrier generation relation with absorption coefficient and flux density of Photons

$$G_{\text{opt}}(y,\lambda) = \alpha(y,\lambda)\,\phi(y,\lambda) \tag{8}$$

where α is the optical absorption coefficient and ϕ is the photon flux density.

The equations to estimate the parameters of the solar cell such as Voc, FF and PCE can be written as

$$V_{oc} = \frac{nkT}{q} \ln\left(\frac{J_{sc}}{J_o} + 1\right) \tag{9}$$

The fill factor (FF) for solar cells is defined by the following equation:

$$FF = \frac{V_{mp} \times J_{mp}}{V_{oc} \times J_{sc}} \tag{10}$$

The equation for power conversion efficiency (PCE) in solar cells is given by:

$$PCE = \frac{p_m}{p_{in}} = \frac{(J_{\mathrm{sc}} \times V_{\mathrm{oc}} \times FF)}{P_{in}} \tag{11}$$

3 Results and Discussion

This study looks into the photoelectric, optical, and thermal stability properties of a set of different photovoltaic solar cells using three different active layers: $Ba_{0.75}Ca_{0.25}TiO_3$, Ba_2CeBiO_6, and Rb_2YCuI_6. Initially, the photosensitization and light-response features of the materials have been examined without electron- and hole-transport layers. Thereafter, their structural stability has been assessed across a range of temperatures. Eventually, a number of solar-cell designs that combine either two or three active layers have been analyzed for their potential to identify optimal configurations that simultaneously provide a certain degree of photovoltaic efficiency while also maintaining thermal stability.

3.1 Single Active-Layer PSCs without Transport Layers

In this part of the work, we have thoroughly studied the optical and electrical characteristics, external quantum efficiency (EQE), photovoltaic behavior, as well as the thermal stability of perovskite solar cells with a single active layer. A comparative analysis was undertaken for the devices, considering different active-layer characteristics and their corresponding photovoltaic outputs. The FTO/perovskite/Au architecture was used to fabricate all the PSCs without the inclusion of additional electron-transport layers or hole-transport layers.

3.1.1 Optoelectronic properties of PSCs

The absorption spectra of all three materials in the UV-visible to IR regions are shown in Figure 3a. All three materials exhibit strong absorption mainly in the UV-visible region. Among them, Rb_2YCuI_6 shows the highest absorption coefficient, with a maximum value of 1.31×10^6 cm^{-1}, while Ba_2CeBiO_6 and $Ba_{0.75}Ca_{0.25}TiO_3$ reach maximum values of 2.23×10^5 cm^{-1} and 1.66×10^5 cm^{-1}, respectively. The higher absorption coefficient of Rb_2YCuI_6 indicates stronger light absorption and is favorable for photovoltaic applications, as efficient absorption can be achieved with a relatively thinner absorber layer. For all three compounds, the absorption coefficient decreases toward longer wavelengths and becomes very small near the visible-to-infrared region. The absorption edges are observed below approximately 600 nm and are associated with electronic transitions between the valence and conduction bands [57]. Overall, Rb_2YCuI_6 exhibits the strongest absorption response among the investigated materials.

The refractive indices of the absorbers are presented in Figure 3b. The refractive index describes how light propagates through a material and relates to its optical polarizability [58]. The static refractive indices are 2.13, 2.14, and 2.62 for Rb_2YCuI_6, Ba_2CeBiO_6, and $Ba_{0.75}Ca_{0.25}TiO_3$, respectively. Their maximum refractive indices in the UV region are 2.69, 2.44, and 3.09, respectively. $Ba_{0.75}Ca_{0.25}TiO_3$ exhibits the highest refractive index over a wide wavelength range, particularly in the visible and infrared regions, indicating a stronger optical response and potentially beneficial light-management properties. Thus, it Rb_2YCuI_6 shows the strongest absorption, whereas it $Ba_{0.75}Ca_{0.25}TiO_3$ exhibits the highest refractive response.

The optical properties of the structures were analyzed with the help of OghmaNano under

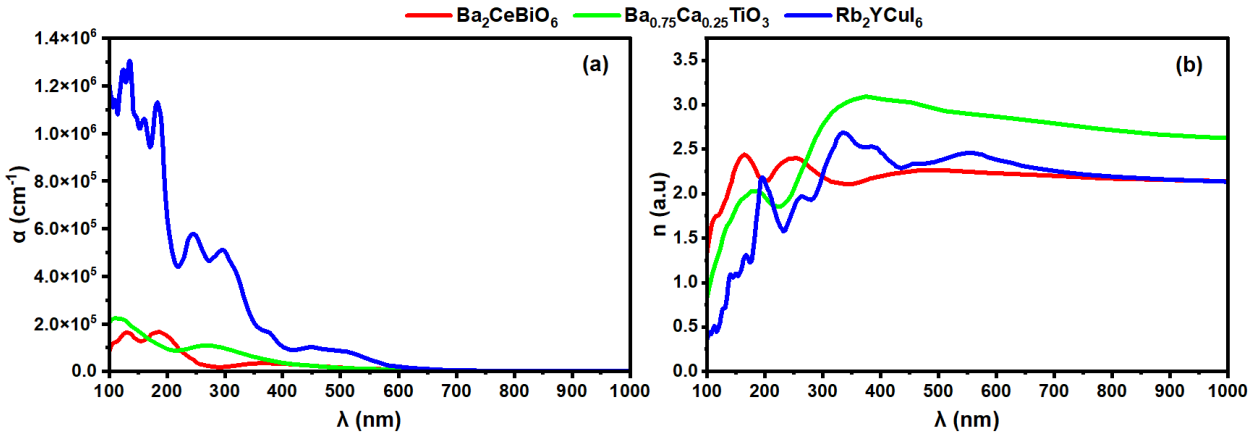


Figure 3: DFT-calculated optical analysis, including the absorption coefficient and refractive index, of the double-oxide perovskite Ba_2CeBiO_6, double-halide perovskite Rb_2YCuI_6, and Ca-doped single perovskite $Ba_{0.75}Ca_{0.25}TiO_3$: (a) absorption coefficient and (b) refractive index. The calculated optical and relevant optoelectronic parameters were incorporated into the OghmaNano simulator as material inputs for the simulation of the proposed new perovskite solar cell structures.

the AM1.5G illumination regime at room temperature (25 °C). In this case, FTO acts as the front contact for incident light, whereas Au acts as the back contact. According to Figure 4a, the transmittance remains significantly low within the 300-900 nm spectral range, with a maximum value of about 5×10^{-3} arbitrary units, indicating that only a very small amount of light is transmitted through the whole structure. The materials Ba_2CeBiO_6 and $Ba_{0.75}Ca_{0.25}TiO_3$ show different transmission peaks near 500 nm. At the same time, $Ba_{0.75}Ca_{0.25}TiO_3$ and Ba_2CeBiO_6 demonstrate an additional peak in the wavelength region of 650-655 nm. On the other hand, the reflectance increases significantly over the 550-600 nm region, with $Ba_{0.75}Ca_{0.25}TiO_3$ exhibiting the highest long-wavelength reflectance as shown in Figure 4b. This is consistent with the obtained DFT optical properties, since the highest refractive index corresponds to $Ba_{0.75}Ca_{0.25}TiO_3$, and hence, a stronger optical response and increased light-matter interaction are expected. Moreover, Rb_2YCuI_6 shows the highest absorption coefficient (1.31×10^6 cm^{-1}), corresponding to the strongest light absorption among the investigated active layers. As a result, the very low transmission of the complete structures can be attributed to the combined effects of the aforementioned optical phenomena.

Spatial distributions of charge carriers generated in Figure 5 can be correlated with the theoretically obtained band gaps of the achieved perovskite materials. Calculated values of the band gap for Ba_2CeBiO_6, $Ba_{0.75}Ca_{0.25}TiO_3$, and Rb_2YCuI_6 compounds are 1.75, 1.775, and 1.67 eV, respectively. The lower band gap of the latter compound means that it has an absorption edge of 700 nm, compared to 600 nm for Ba_2CeBiO_6 and $Ba_{0.75}Ca_{0.25}TiO_3$, respectively. Therefore, the Rb_2YCuI_6 compound may utilize a larger part of the light spectrum and contribute to improved generation of photogenerated carriers. This is confirmed by the high generation rate of carriers close to the illuminated FTO/Rb_2YCuI_6 boundary, which reaches 7×10^{27} cm^{-3} s^{-1} (see Figure 5c). On the other hand, the generation rates of Ba_2CeBiO_6 and $Ba_{0.75}Ca_{0.25}TiO_3$ continue to stay mostly on the level of 2×10^{27} cm^{-3} s^{-1} throughout the majority of the absorber layer. The significant drop in the generation density with the entire thickness Rb_2YCuI_6 suggests that there is considerable

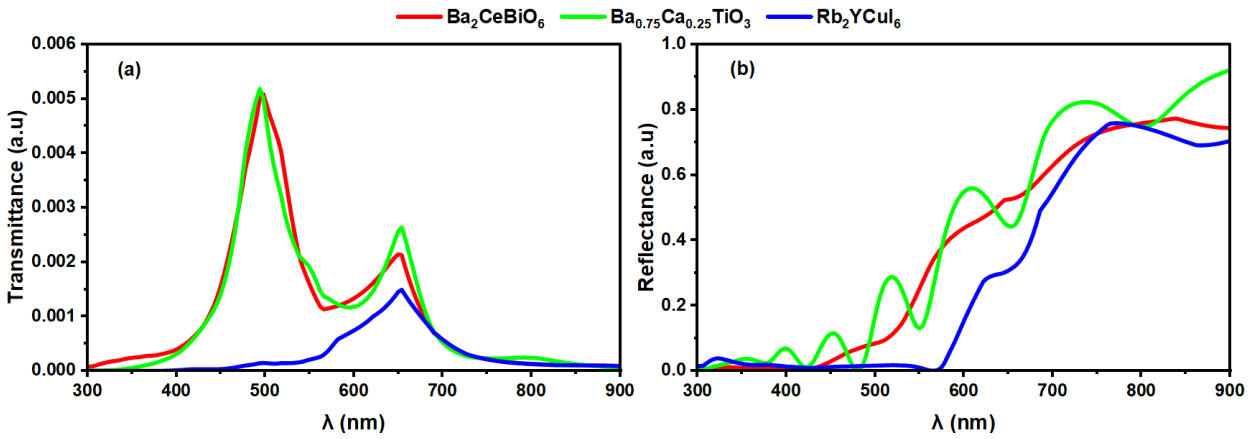
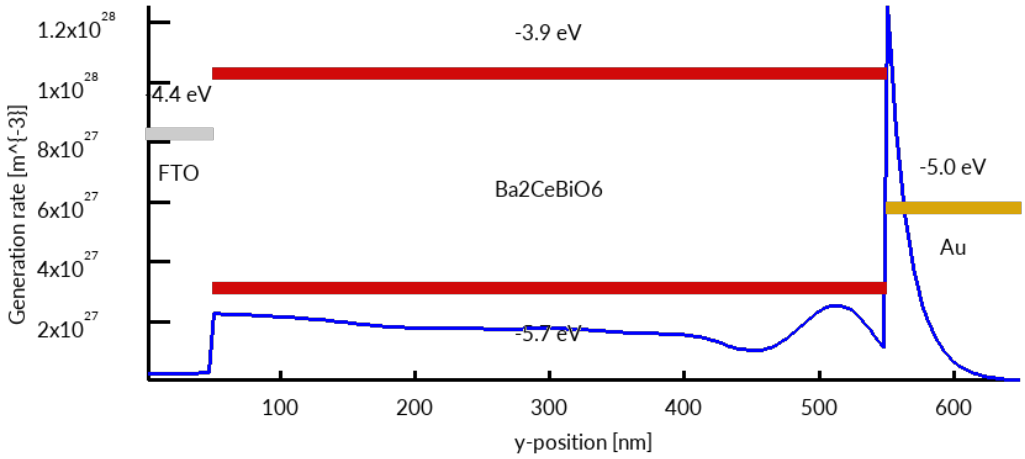
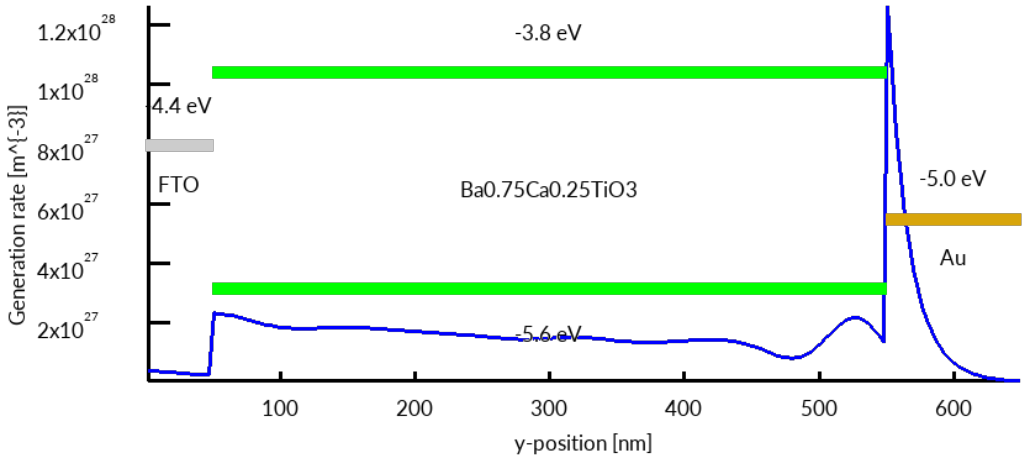


Figure 4: Calculated (a) transmittance and (b) reflectance spectra of FTO/active-layer/Au structures with Ba_2CeBiO_6, $Ba_{0.75}Ca_{0.25}TiO_3$, and Rb_2YCuI_6 under AM1.5G illumination.

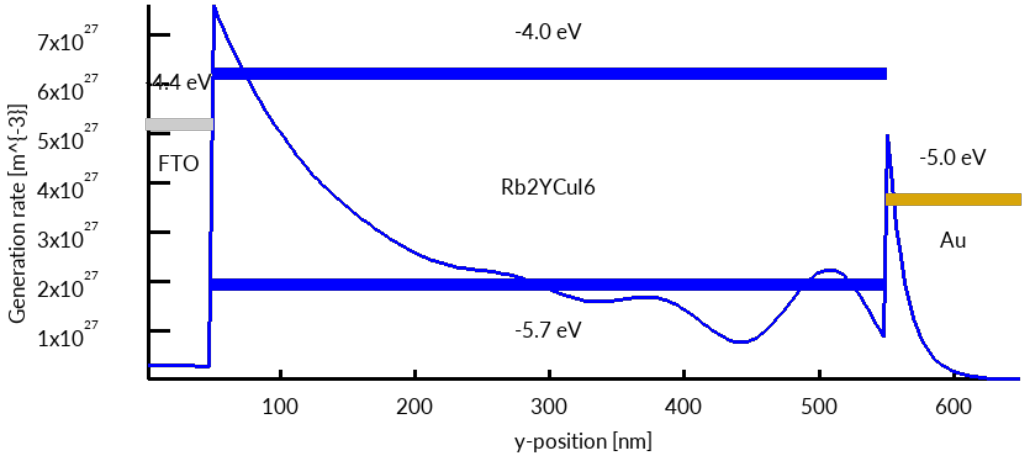
absorption in the illuminated part of the layer, while the almost constant generation densities of Ba_2CeBiO_6 and $Ba_{0.75}Ca_{0.25}TiO_3$ imply that the photogeneration mechanism is less localized in these materials. Still, the increased generation found in Rb_2YCuI_6 cannot be attributed only to its smaller band gap, because the intensity and distribution of photogeneration also depend on the wavelength dependence of the material's absorption coefficient and the optical field inside the active layer.



(a) FTO/Ba_2CeBiO_6/Au



(b) FTO/$Ba_{0.75}Ca_{0.25}TiO_3$/Au



(c) FTO/Rb_2YCuI_6/Au

Figure 5: Spatial distribution of the photocarrier generation rate within the active layers of the simulated FTO/perovskite/Au solar-cell structures obtained from OghmaNano: (a) FTO/Ba_2CeBiO_6/Au, (b) FTO/$Ba_{0.75}Ca_{0.25}TiO_3$/Au, and (c) FTO/Rb_2YCuI_6/Au. The FTO, perovskite, and Au layer thicknesses are 50, 500, and 100 nm, respectively.

3.1.2 Efficiency and Performance of PSCs

The performance of the photovoltaic cells based on the FTO/active-layer/Au structures was also evaluated in terms of their J–V characteristics and quantum efficiency (QE), which are shown in Figures 6 and 7, respectively. In the absence of an electron transport layer (ETL) and a hole transport layer (HTL), photogenerated carriers are extracted directly through the interfaces between the active layer and the FTO and Au electrodes. As shown in Table 2, the system based on Rb_2YCuI_6 produces the highest short-circuit current density, J_{SC}, of $17.599\ mA.cm^{-2}$, while Ba_2CeBiO_6 and $Ba_{0.75}Ca_{0.25}TiO_3$ exhibit values of 11.995 and $4.997\ mA.cm^{-2}$, respectively. In contrast, $Ba_{0.75}Ca_{0.25}TiO_3$ shows the highest open-circuit voltage, V_{OC}, and fill factor (FF), with values of 1.37 V and 89.15%, respectively. However, its relatively low photocurrent results in a PCE of only 6.09%. The Rb_2YCuI_6-based device achieves the highest PCE of 15.53%, mainly owing to its substantially higher J_{SC}, despite its lower V_{OC} and FF.

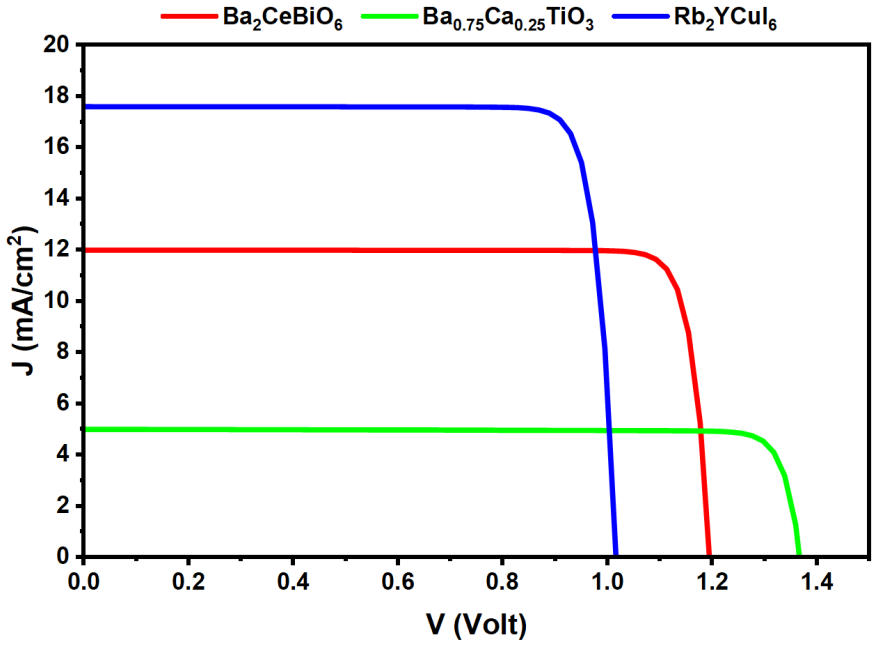


Figure 6: Current density-voltage (J-V) characteristics of the photovoltaic cells based on different active-layer material structures: Ca-doped single perovskite $Ba_{0.75}Ca_{0.25}TiO_3$ (green line), double-halide perovskite Rb_2YCuI_6 (blue line), and double-oxide perovskite Ba_2CeBiO_6 (red line), sandwiched between the FTO and Au contact layers without ETL and HTL materials, as simulated using OghmaNano software.

The QE spectra follow a similar trend, with Rb_2YCuI_6 exhibiting the highest QE over a broad region of the visible spectrum, consistent with its highest calculated absorption coefficient of $1.31 \times 10^6\ cm^{-1}$. The strong optical absorption therefore promotes photon harvesting and contributes to the higher photocurrent. However, the QE decreases in the 650–900 nm wavelength range, which may be associated with increased surface reflection and enhanced carrier recombination. In addition, the higher J_{SC} values obtained for the double-perovskite materials, particularly Rb_2YCuI_6 and Ba_2CeBiO_6, can be related to their calculated carrier mobility and carrier concentration, as described by Equations (1)–(4). These electronic properties can facilitate charge transport and contribute to more efficient carrier collection. Conversely, despite its high refractive index, $Ba_{0.75}Ca_{0.25}TiO_3$ exhibits a relatively low photocurrent, which is associated with its low

QE over most of the investigated spectral range. Overall, the photovoltaic performance of the cells without ETL and HTL is strongly influenced by the optical absorption, QE response, optical losses, and electronic transport properties of the active layer.

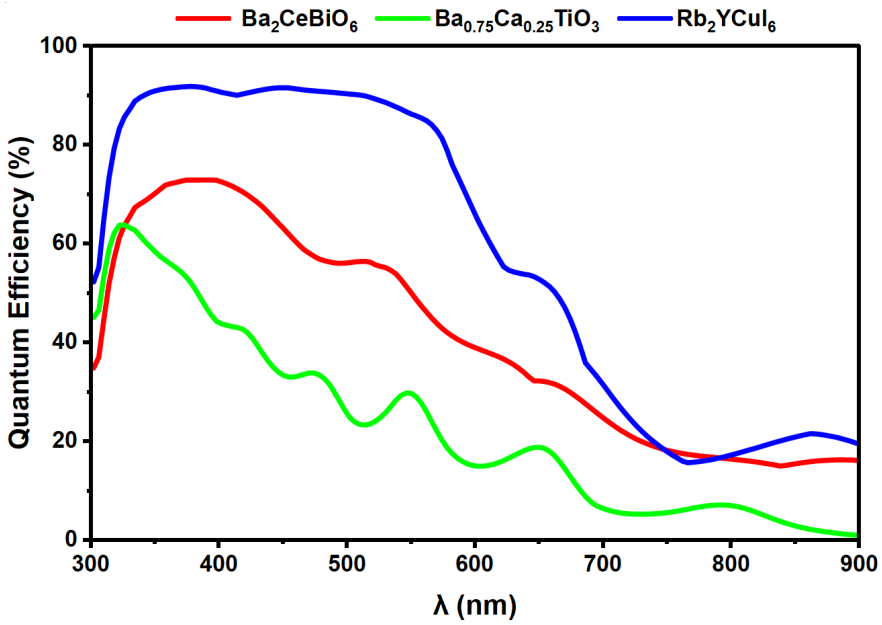


Figure 7: Quantum efficiency (QE) of Ba_2CeBiO_6, Rb_2YCuI_6, and $Ba_{0.75}Ca_{0.25}TiO_3$ as a function of wavelength in the range of 300-900 nm.

Table 2: Photovoltaic performance parameters of the perovskite solar cells without electron and hole transport layers, with different active-layer materials sandwiched between the two contact layers. The thickness of the perovskite active layer is fixed at 500 nm for all cells.

Parameters	**Ba_2CeBiO_6**	**$Ba_{0.75}Ca_{0.25}TiO_3$**	**Rb_2YCuI_6**
Jsc (mA/cm^2)	11.995	4.997	17.599
Voc (Volt)	1.19	1.37	1.02
FF %	88.74	89.15	86.87
PCE %	12.71	6.09	15.53

3.1.3 Thermal stability of PSCs

The temperature dependence of the photovoltaic parameters for the three perovskite materials is illustrated in Figure 8 for the FTO/perovskite/Au structure without ETL and HTL layers. With increasing temperature from 300 to 325 K, the open-circuit voltage (V_{OC}) decreases for all three materials. This behavior can be attributed to the temperature dependence of the band gap and the increase in intrinsic carrier concentration, which enhances the reverse saturation current and consequently reduces V_{OC}, as described by Equation(9).

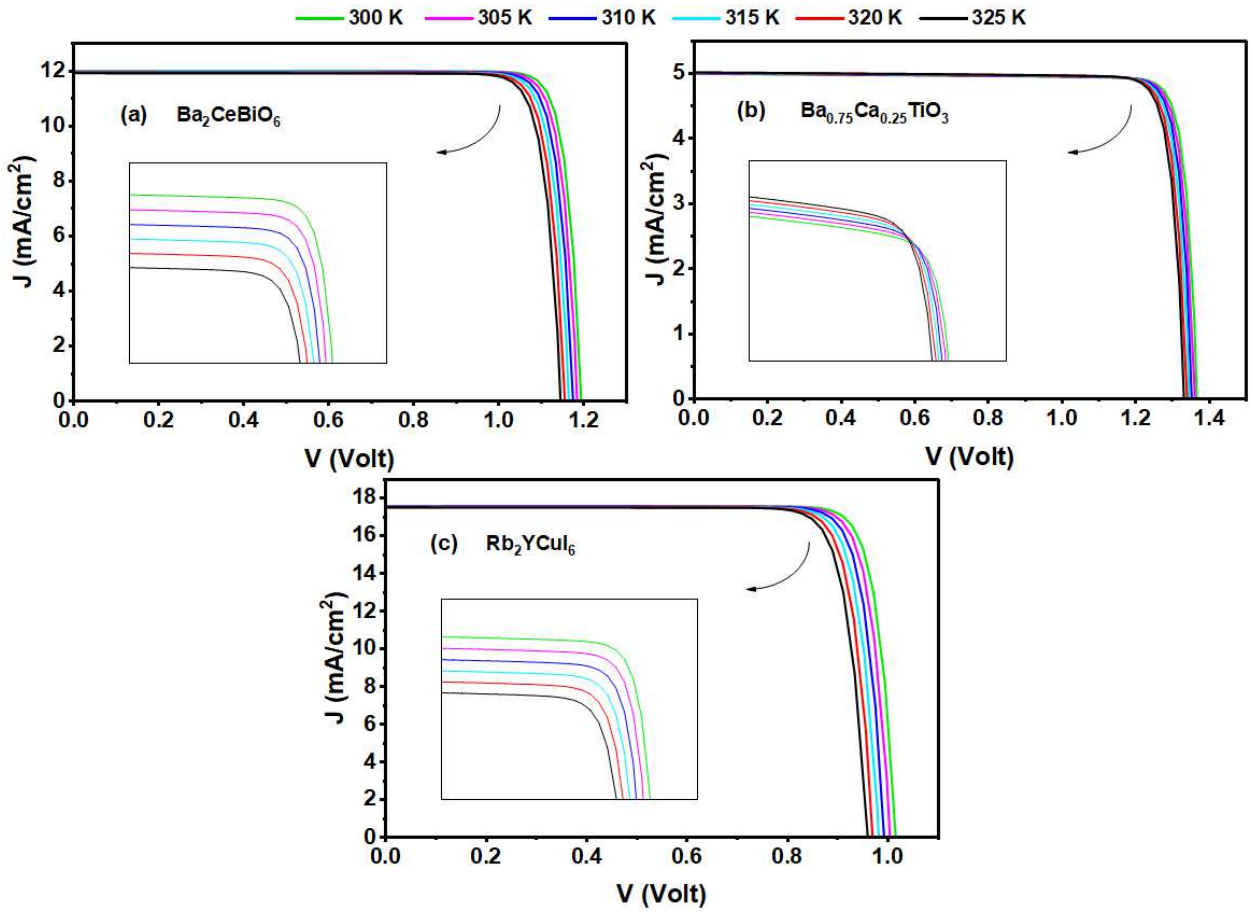


Figure 8: Current density–voltage (J–V) characteristics of the perovskite solar cells at temperatures ranging from 300 to 325 K: (a) FTO/Ba_2CeBiO_6/Au, (b) FTO/$Ba_{0.75}Ca_{0.25}TiO_3$/Au, and (c) FTO/Rb_2YCuI_6/Au.

On the other hand, a different temperature dependence is observed for the short-circuit current density (J_{SC}). The J_{SC} of Rb_2YCuI_6 and Ba_2CeBiO_6 decreases slightly with increasing temperature, whereas a slight increase in J_{SC} is observed for $Ba_{0.75}Ca_{0.25}TiO_3$. This behavior may be related to the relatively high dielectric constant of $Ba_{0.75}Ca_{0.25}TiO_3$, which can reduce the Coulombic interaction between electrons and holes and thereby favor charge separation and collection. As shown in Figure 9, the normalized values of V_{OC} and FF decrease with increasing temperature, whereas J_{SC} remains relatively stable.

At 325 K, the normalized PCE values are approximately 0.97, 0.94, and 0.925 for $Ba_{0.75}Ca_{0.25}TiO_3$, Ba_2CeBiO_6, and Rb_2YCuI_6, respectively. Therefore, the corresponding PCE losses from 300 to 325 K are approximately 3%, 6%, and 7.5%, respectively. The smaller slope of the normalized PCE line for $Ba_{0.75}Ca_{0.25}TiO_3$ indicates that it exhibits the best thermal stability among

the three materials. In comparison, Ba_2CeBiO_6 shows intermediate stability, while Rb_2YCuI_6 exhibits the strongest degradation with increasing temperature. The enhanced thermal stability of $Ba_{0.75}Ca_{0.25}TiO_3$ may also be associated with Ca substitution, which can modify the defect structure and potentially reduce detrimental defect states and temperature-sensitive recombination.

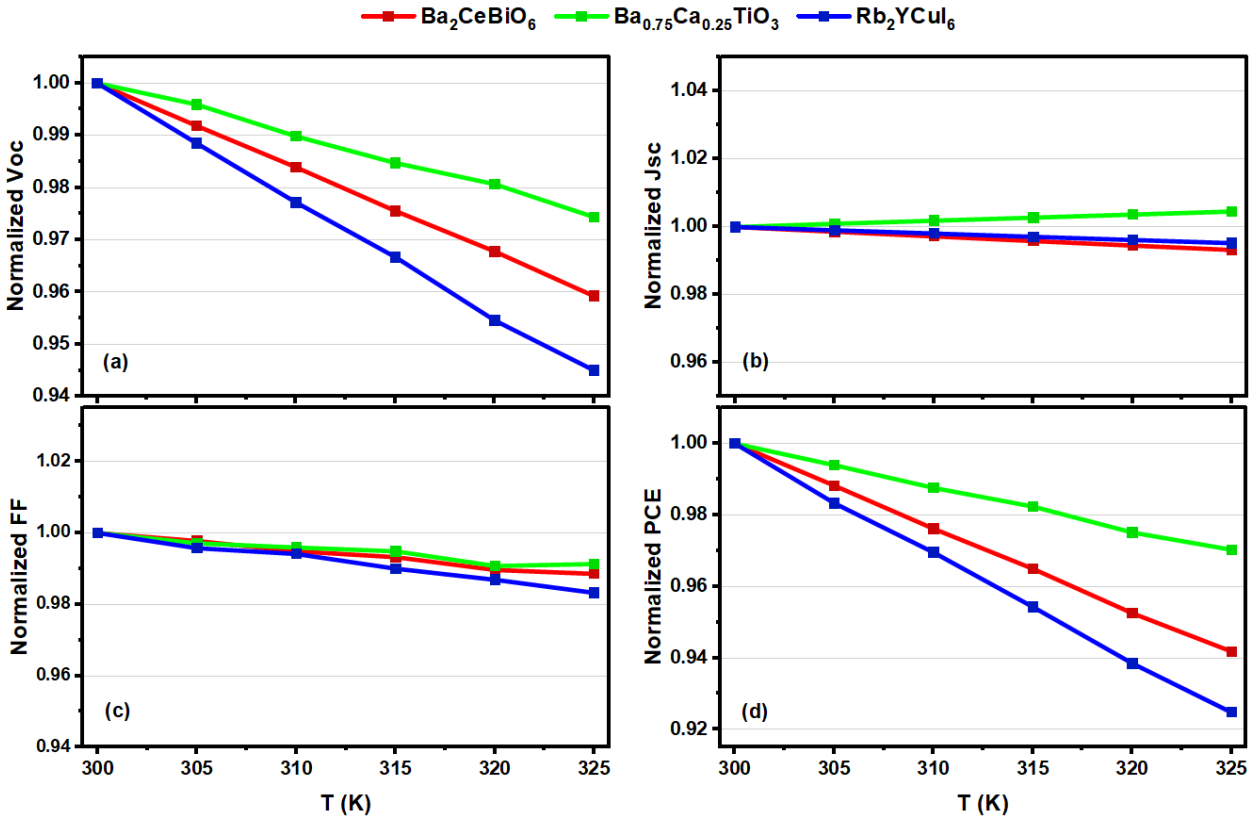


Figure 9: Temperature dependence of the normalized photovoltaic parameters of the three perovskite solar cells from 300 to 325 K: (a) V_{OC}, (b) J_{SC}, (c) FF, and (d) PCE. The parameters are normalized to their respective values at 300 K.

3.2 Double Active-Layer PSCs without Transport Layers

3.2.1 Efficiency and Performance of PSCs

The simulated photovoltaic results show a strong dependence of device performance on the composition and arrangement of the perovskite bilayer. Herein, all simulated results are applied at room temperature without ETL and HTL layers between the FTO and Au contact, while each active layer has a constant thickness of 500 nm. For the FTO/Rb_2YCuI_6/Ba_2CeBiO_6/Au structure, the following photovoltaic parameters were obtained: a short-circuit current density (J_{SC}) of 22.965 mA/cm^2, an open-circuit voltage (V_{OC}) of 1.12 V, a fill factor (FF) of 87.73%, and a power conversion efficiency (PCE) of 22.64%. But the FTO/$Ba_{0.75}Ca_{0.25}TiO_3$/Rb_2YCuI_6/Au structure exhibited a slightly higher open-circuit voltage of 1.15 V; however, its short-circuit current density was lower, at 21.797 mA/cm^2, and its fill factor was significantly reduced to 76.51% (see Table 3 and Figure 10). In comparison for the FTO/Ba_2CeBiO_6/Rb_2YCuI_6/Au and FTO/Rb_2YCuI_6/$Ba_{0.75}Ca_{0.25}TiO_3$/Au structures, the corresponding photovoltaic parameters were obtained as follows: short-circuit current densities (J_{SC}) of 23.399 and 22.0796 mA/cm^2, open-

circuit voltages (V_{OC}) of 1.11 and 1.14 V, fill factors (FF) of 87.66% and 87.24%, and power conversion efficiencies (PCE) of 22.69% and 21.92%, respectively.

Table 3: Photovoltaic performance parameters of the perovskite solar cells without electron and hole transport layers, with double active-layer materials sandwiched between the two contact layers, FTO and Au. The thickness of the perovskite active layer is fixed at 500 nm for all cells.

Device Structure	**Jsc (mA/cm^2)**	**Voc (Volt)**	**FF %**	**PCE %**
Ba_2CeBiO_6/Rb_2YCuI_6	23.399	1.11	87.66	22.69
Rb_2YCuI_6/Ba_2CeBiO_6	22.965	1.12	87.73	22.64
$Rb_2YCuI_6/Ba_{0.75}Ca_{0.25}TiO_3$	22.0796	1.14	87.24	21.92
$Ba_{0.75}Ca_{0.25}TiO_3/Rb_2YCuI_6$	21.797	1.15	76.51	19.19

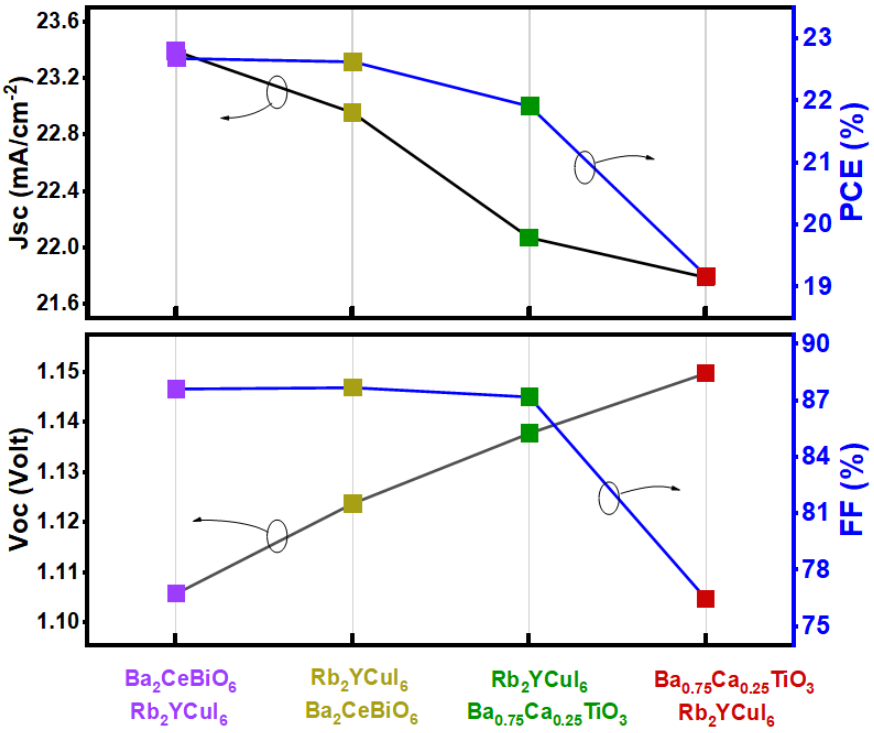


Figure 10: Efficiency parameters of the perovskite solar cells based on a perovskite bilayer: (a) Jsc, (b) Voc, (c) FF, (d) PCE, at a temperature of 300 K.

This behavior is further supported by the spectral response, in which the Ba_2CeBiO_6/Rb_2YCuI_6 configuration maintains a relatively high quantum efficiency (more than 95%) over a broad portion of the UV-visible spectrum (from 325 to 625 nm) as shown in Figure 11b. Then, beyond 625 nm and up to 900 nm, the quantum efficiency gradually decreased, reaching approximately 30%, due to the reduced charge-carrier generation within the cell structures in this spectral region, thereby contributing to enhanced photocurrent generation (see Figure 12a). The charge-carrier generation profiles also show distinct spectral characteristics for the two configurations.

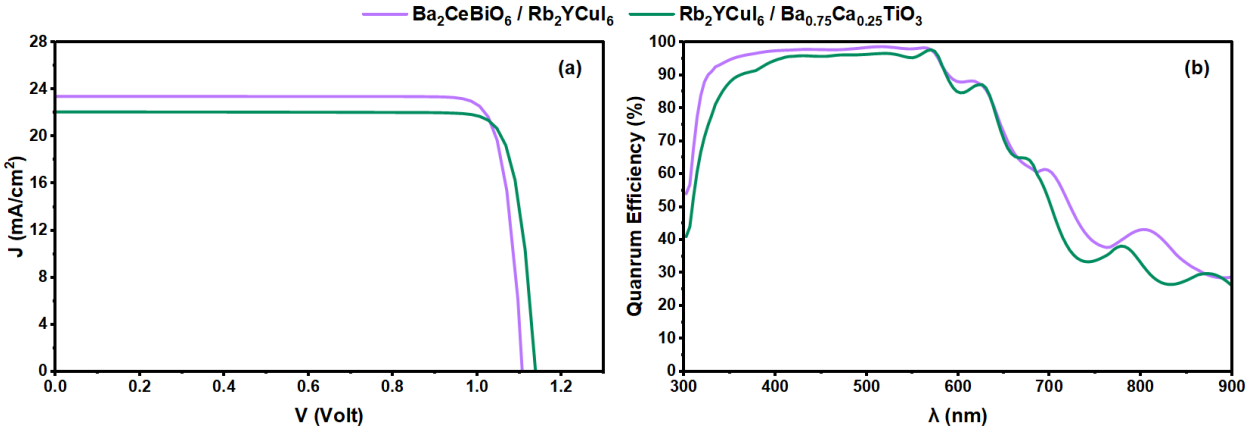


Figure 11: Current density–voltage (J–V) characteristics and (b) quantum efficiency of the perovskite solar cells with the two device structures: FTO/Ba_2CeBiO_6/Rb_2YCuI_6/Au and FTO/Rb2YCuI6/Ba0.75Ca0.25TiO_3/Au.

3.2.2 Charge carrier generation and recombination of PSCs

For the Ba_2CeBiO_6/Rb_2YCuI_6 structure, the charge-carrier generation rate reaches a maximum of approximately 22.5×10^{24} m^{-3} s^{-1} at around 400 nm. In contrast, the Rb_2YCuI_6/$Ba_{0.75}Ca_{0.25}TiO_3$ structure exhibits a considerably higher maximum generation rate of approximately 38×10^{24} m^{-3} s^{-1} near 620 nm, with additional peaks of approximately 28×10^{24} m^{-3} s^{-1} at 550 nm and 20×10^{24} m^{-3} s^{-1} around 700 nm. These results indicate that the two bilayer cell configurations have different spectral distributions of photogenerated carriers. Nevertheless, the higher peak generation rate of the Rb_2YCuI_6/$Ba_{0.75}Ca_{0.25}TiO_3$ structure does not result in a higher J_{SC}, indicating that the overall photocurrent depends not only on the magnitude of carrier generation at individual wavelengths but also on the spectral distribution and subsequent carrier collection.

Additionally, from Figure 12b, the simulated recombination-rate profiles show a significantly lower carrier recombination rate in the Ba_2CeBiO_6/Rb_2YCuI_6 configuration compared with the Rb_2YCuI_6/$Ba_{0.75}Ca_{0.25}TiO_3$ configuration. At a carrier concentration of approximately 0.05×10^{21} m^{-3}, the recombination rate for the Ba_2CeBiO_6/Rb_2YCuI_6 structure is approximately zero rate, whereas that of the Rb_2YCuI_6/$Ba_{0.75}Ca_{0.25}TiO_3$ structure is approximately 2×10^{-16} $m^{-3}s^{-1}$. At higher carrier concentrations, the recombination rate remains approximately 0.5×10^{-16} m^{-3} s^{-1} for the Rb_2YCuI_6/$Ba_{0.75}Ca_{0.25}TiO_3$ configuration. These results demonstrate substantially stronger recombination losses in the Rb_2YCuI_6/$Ba_{0.75}Ca_{0.25}TiO_3$ configuration, particularly at low-to-moderate carrier concentrations.

The total charge-density profiles further support this interpretation as shown in Figure 12c. At 0 V, the total charge density is approximately 0.52×10^{21} m^{-3} for the Ba_2CeBiO_6/Rb_2YCuI_6 structure and approximately 0.95×10^{21} m^{-3} for the Rb_2YCuI_6/$Ba_{0.75}Ca_{0.25}TiO_3$ structure. At approximately 1.0 V, the charge density increases to approximately 0.8×10^{21} m^{-3} and 1.4×10^{21} m^{-3}, respectively. With increasing voltage, the difference becomes more pronounced. At 1.6 V, the charge density reaches approximately more than 2.5×10^{21} m^{-3} for the Ba_2CeBiO_6/Rb_2YCuI_6 configuration and 3.0×10^{21} m^{-3} for the Rb_2YCuI_6/$Ba_{0.75}Ca_{0.25}TiO_3$ configuration. The higher charge density in the latter structure indicates greater carrier accumulation, which, when considered together with its higher recombination rate, suggests less effective carrier extraction and increased carrier losses

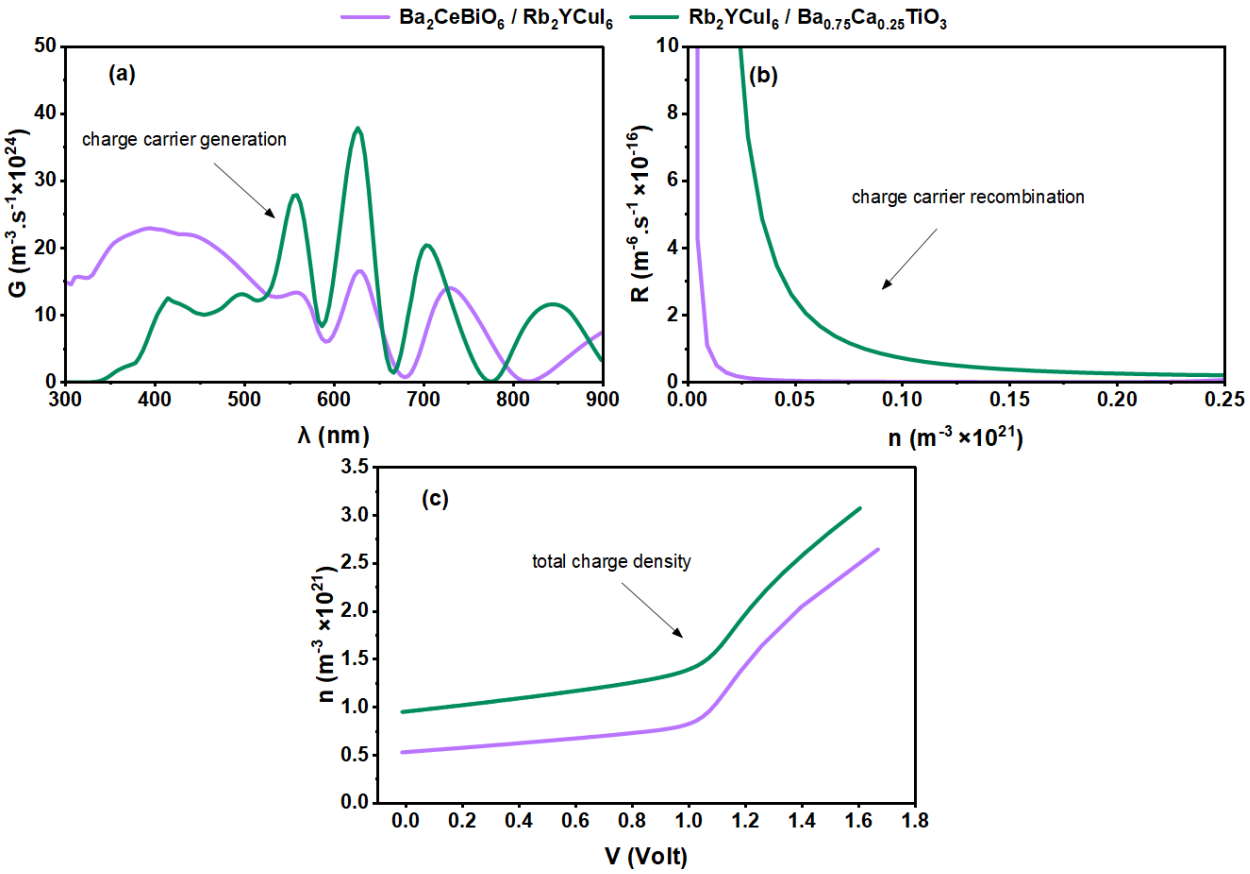


Figure 12: (a) Charge carrier generation, (b) charge carrier recombination, and (c) charge carrier density in double-active-layer perovskite solar cells.

within the device, especially for the cells without transport layers. This behavior is consistent with its lower fill factor and photocurrent. Therefore, these findings suggest that the higher PCE of the Ba_2CeBiO_6/Rb_2YCuI_6 without ETL and HTL layers configuration is primarily associated with more efficient carrier collection and reduced recombination losses rather than being solely determined by the V_{OC}.

As illustrated by the photon absorption distribution in Figure 13, the absorption profile is closely related to the carrier-generation rate described by Equation 8. At shorter wavelengths, stronger photon absorption occurs near the illuminated surface, resulting in higher carrier generation. In contrast, longer-wavelength photons penetrate more deeply into the material, leading to lower generation rates. For the FTO/Ba_2CeBiO_6/Rb_2YCuI_6/Au structure, the two maximum generation rates are approximately 1.5×10^{34} $m^{-3}s^{-1}$ and 0.6×10^{34} $m^{-3}s^{-1}$, occurring mainly within the Ba_2CeBiO_6 and Rb_2YCuI_6 layers at depths of approximately 200 nm and 600 nm, respectively, over the wavelength range of 300-600 nm. Also, for the other device, the generation profile within the 600-900 nm thickness range remains moderate over the 350-600 nm wavelength range. This indicates relatively limited carrier generation in this region, suggesting that the device may benefit from the incorporation of a hole-transport layer (HTL) to facilitate the extraction of accumulated holes toward the back contact and thereby reduce leakage current.

In contrast, the FTO/Rb2YCuI6/$Ba0.75Ca0.25TiO_3$/Au structure exhibits a substantially higher peak generation rate of approximately 3.2×10^{34} $m^{-3}s^{-1}$, concentrated mainly within the Rb_2YCuI_6

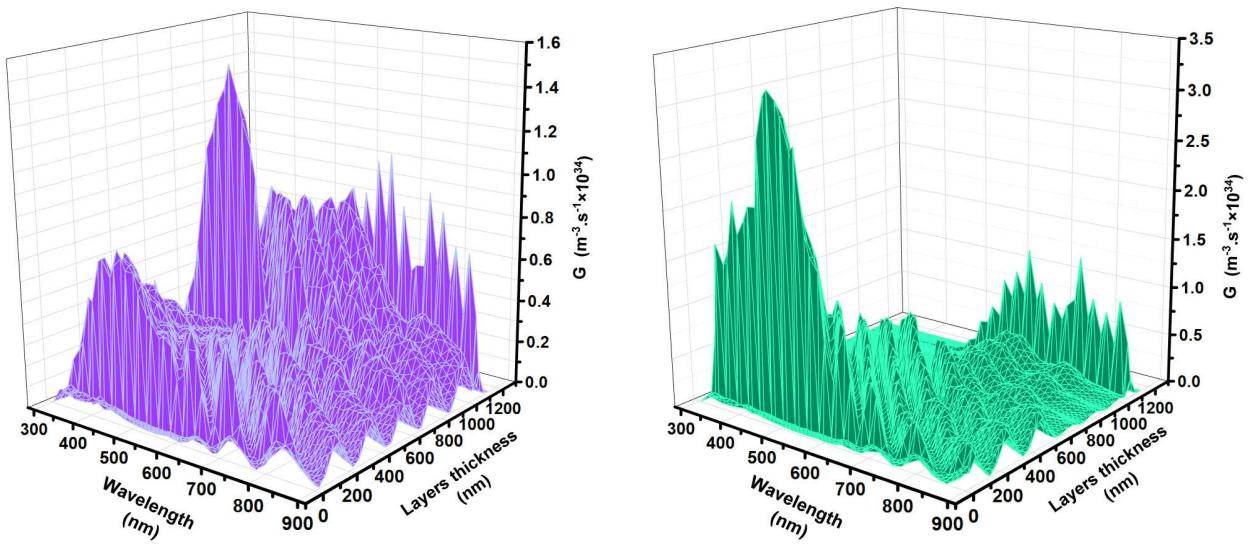


Figure 13: Generation rate of charge carriers as function of device thickness and incident light wavelength for both (a) Ba_2CeBiO_6/Rb_2YCuI_6 (b) $Rb_2YCuI_6/Ba_{0.75}Ca_{0.25}TiO_3$ PSCs.

layer at depths of approximately 150-350 nm and over the wavelength range of 300-600 nm. This indicates a high carrier-generation rate near the FTO/Rb_2YCuI_6 interface. The strong carrier generation near the front contact suggests that incorporating an electron-transport layer (ETL) may facilitate more efficient electron extraction toward the front contact and help reduce carrier accumulation and leakage current. Figure 14 shows the dependence of the short-circuit current density (J_{SC}) and open-circuit voltage (V_{OC}) of the two perovskite bilayer solar cells, Ba_2CeBiO_6/Rb_2YCuI_6 and Rb_2YCuI_6/ $Ba_{0.75}Ca_{0.25}TiO_3$, on the illumination intensity. As the light intensity increases, both the short-circuit current density (J_{SC}) and open-circuit voltage (V_{OC}) increase for both structures. Figure 14(a) shows that the increase in J_{SC} with increasing light intensity is more significant for the Ba_2CeBiO_6/Rb_2YCuI_6 structure than for the $Rb_2YCuI_6/Ba_{0.75}Ca_{0.25}TiO_3$ structure. The nearly proportional increase in J_{SC}, represented by the almost linear curve in Figure 14(a), indicates efficient photocarrier generation and collection as the illumination intensity increases.

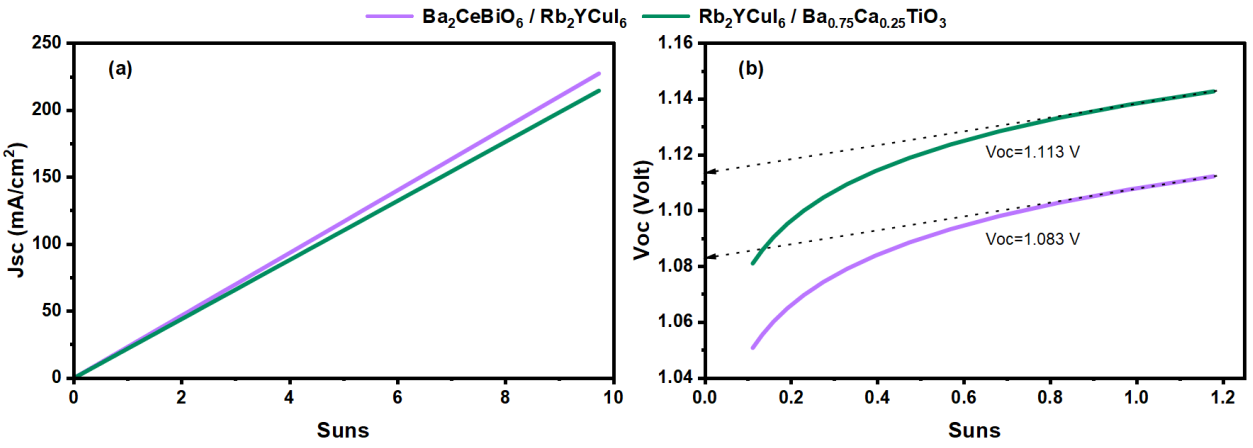


Figure 14: Dependence of (a) short-circuit current density (J_{SC}) and (b) open-circuit voltage (V_{OC}) on illumination intensity for the Ba_2CeBiO_6/Rb_2YCuI_6 and $Rb_2YCuI_6/Ba_{0.75}Ca_{0.25}TiO_3$ perovskite solar cells.

In contrast, the $Rb_2YCuI_6/Ba_{0.75}Ca_{0.25}TiO_3$ structure exhibits a higher open-circuit voltage (V_{OC}), reaching 1.143 V, compared with 1.112 V for the Ba_2CeBiO_6/Rb_2YCuI_6 structure at the highest illumination intensity (see Figure 14b). At illumination intensities above approximately 0.8 suns, V_{OC} exhibits an approximately linear dependence on the logarithm of the illumination intensity. As discussed previously, the dominant recombination mechanism in the solar cell can be evaluated using the diode ideality factor, which is determined from the dependence V_{OC} on the logarithm of the light intensity. Ideality factors close to 1 indicate a dominant contribution from radiative recombination, whereas values approaching 2 suggest a greater contribution from trap-assisted Shockley–Read–Hall (SRH) recombination.

3.2.3 Thermal stability of double active layers-based PSCs

Figures 15 and 16 illustrate the influence of temperature on the photovoltaic performance of the two perovskite-bilayer based PSC structures, Ba_2CeBiO_6/Rb_2YCuI_6 and $Rb_2YCuI_6/Ba_{0.75}Ca_{0.25}TiO_3$, over the temperature range of 300–330 K. Figure 15 shows that, as the temperature increases, the $J-V$ curves gradually shift toward lower voltages. As a result, both structures experience a decrease in V_{OC}.

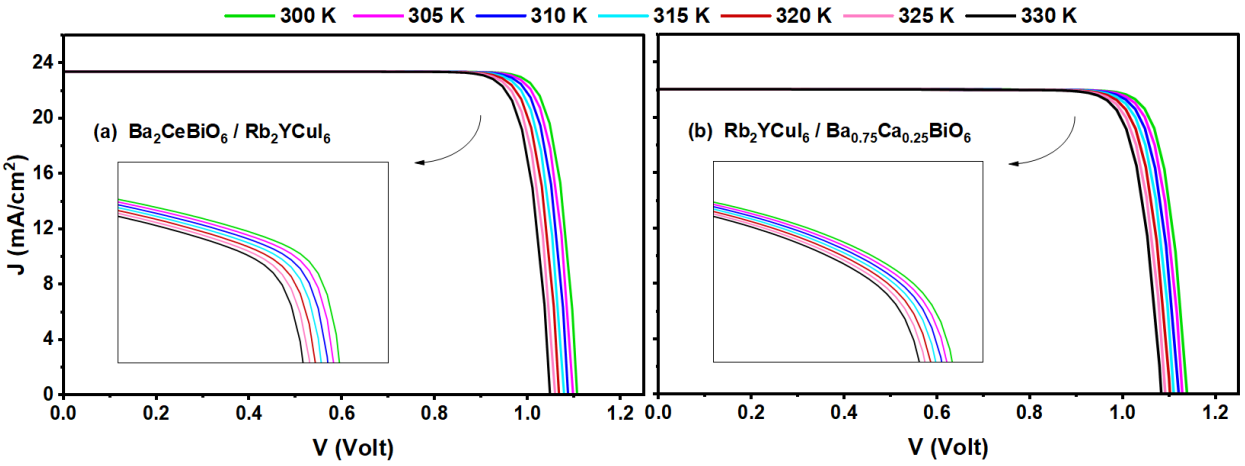


Figure 15: Temperature stability of JV characteristics for the Ba_2CeBiO_6/Rb_2YCuI_6 (a) and $Rb_2YCuI_6/Ba_{0.75}Ca_{0.25}TiO_3$ (b) perovskite solar cells.

The normalized parameters in Figure 16 reveal that V_{OC} continuously decreases with increasing temperature, while J_{SC} remains nearly unchanged. Moreover, the FF remains relatively high over the investigated temperature range, particularly between 300 and 315 K. Both structures exhibit nearly the same V_{OC} and PCE at approximately 320 K. As shown in Figure 16d, the PCE gradually decreases with increasing temperature, reaching its minimum value at 330 K. This decrease is mainly attributed to the reduction in V_{OC}. At 330 K, the normalized PCE decreases to approximately 0.93 for Ba_2CeBiO_6/Rb_2YCuI_6 and 0.937 for $Rb_2YCuI_6/Ba_{0.75}Ca_{0.25}TiO_3$. Overall, both structures demonstrate good performance and relatively stable behavior over the investigated temperature range. However, the $Rb_2YCuI_6/Ba_{0.75}Ca_{0.25}TiO_3$ perovskite bilayer exhibits slightly better thermal stability than Ba_2CeBiO_6/Rb_2YCuI_6.

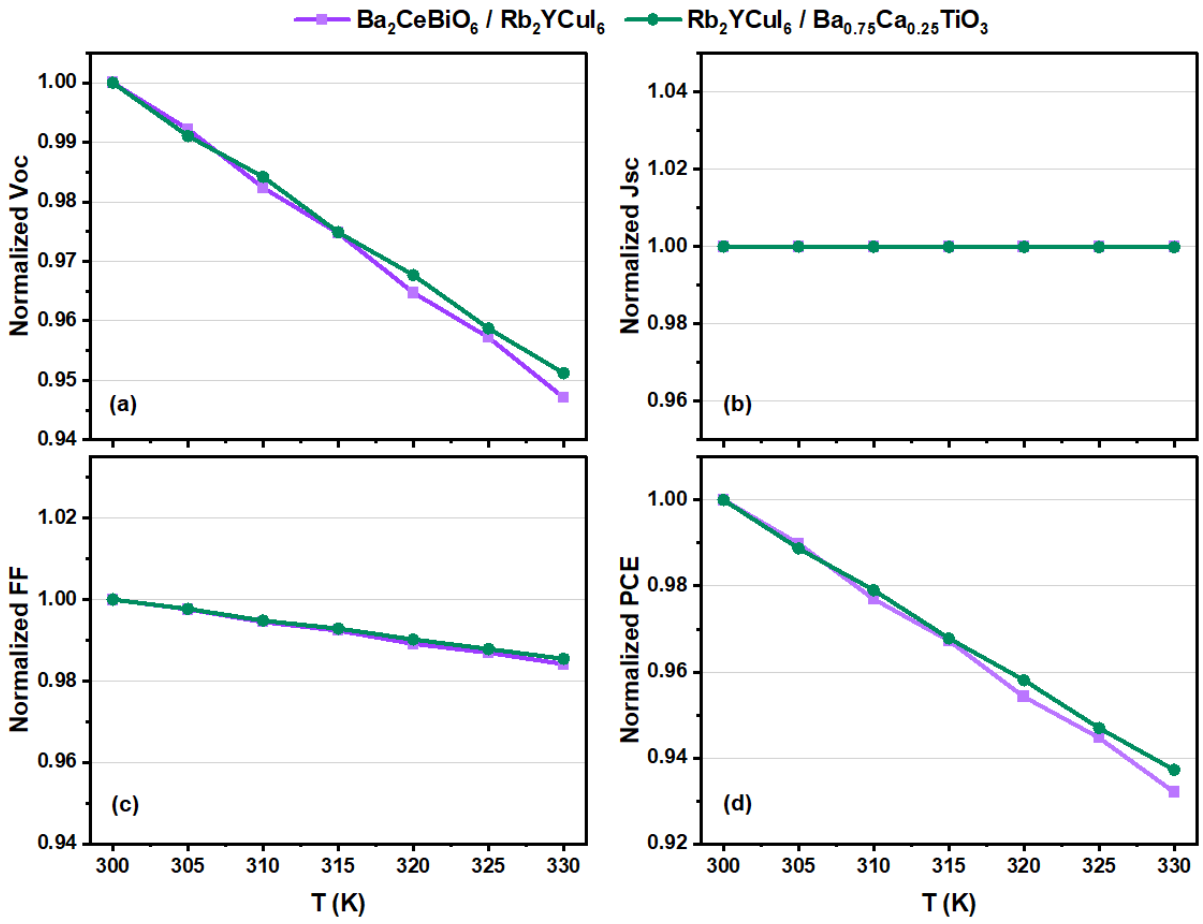


Figure 16: Temperature stability of normalized efficiency parameters for the Ba_2CeBiO_6/Rb_2YCuI_6 and $Rb_2YCuI_6/Ba_{0.75}Ca_{0.25}TiO_3$ perovskite solar cells: (a) Voc, (b) Jsc, (c) FF, and (d) PCE.

4 Conclusion

This study investigated the photovoltaic performance, optical properties, charge-carrier behavior, and thermal stability of $Ba_{0.75}Ca_{0.25}TiO_3$, Ba_2CeBiO_6, and Rb_2YCuI_6 using DFT-derived parameters and OghmaNano simulations. Single-layer devices were modeled using an FTO/perovskite/Au structure without electron transport layers (ETL) or hole transport layers (HTL). All three materials exhibited strong UV–visible absorption. Rb_2YCuI_6 showed the highest absorption coefficient, approximately 1.31×10^6 cm^{-1}, and achieved the highest individual power conversion efficiency (PCE) of 15.53%, primarily due to its high short-circuit current density (J_{sc}) of 17.599 mA/cm^2. $Ba_{0.75}Ca_{0.25}TiO_3$ exhibited the highest open-circuit voltage (V_{oc}) of 1.37 V and fill factor (FF) of 89.15%, but its PCE was limited to 6.09% by its lower photocurrent. It also demonstrated the best thermal stability among the single-layer devices, with only approximately 3% PCE loss between 300 and 325 K. The bilayer structures provided improved photovoltaic performance. In particular, the Ba_2CeBiO_6/Rb_2YCuI_6 configuration achieved a PCE of 22.64%, with $J_{sc} = 22.965$ mA/cm^2, $V_{oc} = 1.12$ V, and FF = 87.73%. This enhancement was attributed to more efficient carrier collection and reduced recombination losses. Both bilayer structures (Ba_2CeBiO_6/Rb_2YCuI_6 and Rb_2YCuI_6/$Ba_{0.75}Ca_{0.25}TiO_3$) maintained good thermal stability up to 330 K, with normalized PCE values of approximately 0.93 and 0.937, respectively. Overall, perovskite-perovskite interface engineering offers a promising approach for enhancing photovoltaic performance and thermal stability. Future studies should optimize layer thicknesses, incorporate suitable ETL/HTL materials, and experimentally validate the most promising device structures.

Clinical Trial Registration

We confirm that our study is not a clinical trial; therefore, clinical trial registration is not applicable.

Funding Declaration

The authors received no funding for the conduct of this study or the preparation of this manuscript.

Ethics

Ethics consent to Participate, and Consent to Publish declarations: not applicable.

Acknowledgements

Darko A. Noori and Eman Qabil Majeed gratefully acknowledges all the support for this study from the Ministry of Higher Education and Scientific Research, Kurdish National Research Council (KNRC), Kurdistan Regional Government, and the University of Sulaimani.

Author contribution

Darko A. Noori and Eman Qabil Majeed certify that they have participated sufficiently in the work to take public responsibility for its content. Both authors contributed to the conception, design, analysis, writing, and/or revision of the manuscript.

Data availability

Darko A. Noori and Eman Qabil Majeed certifies that they have participated sufficiently in the work to take public responsibility for the content, including participation in the manuscript's concept, design, analysis, writing, or revision. Furthermore, the author certifies that this material or similar material has not been and will not be submitted to or published in any other publication.

Declarations

Conflict of interest the authors declare no competing interests.

References

[1] T. Kirchartz, J. Bisquert, I. Mora-Sero, and G. Garcia-Belmonte, "Classification of solar cells according to mechanisms of charge separation and charge collection," *Physical Chemistry Chemical Physics*, 1 2015.

[2] A. A. Firoozi, A. A. Firoozi, and M. R. Maghami, "Harnessing photovoltaic innovation: Advancements, challenges, and strategic pathways for sustainable global development," *Energy Conversion and Management: X*, 7 2025.

[3] A. O. Ali *et al.*, "Advancements in photovoltaic technology: A comprehensive review of recent advances and future prospects," *Energy Conversion and Management: X*, 4 2025.

[4] S. B. Andjela, "Application of photovoltaic technology in the use of solar energy," *Annals of Environmental Science and Toxicology*, pp. 094–098, 8 2021.

[5] P. Sharma and R. K. Mishra, "Comprehensive study on photovoltaic cell's generation and factors affecting its performance: A review," *International Journal of Energy and Environmental Engineering*, 4 2025.

[6] B. G. Akinoglu, B. Tuncel, and V. Badescu, "Beyond 3rd generation solar cells and the full spectrum project. recent advances and new emerging solar cells," *Sustainable Energy Technologies and Assessments*, vol. 46, p. 101287, 8 2021.

[7] M. L. Yerima, I. Muhammad, and A. B. Gambo, "Generation of solar cells: A review of materials, operation and limitation of photovoltaic technologies," *Nile Journal of Engineering & Applied Science*, 2025.

[8] S. Gupta, S. Singh, R. R. Chaudhary, DeepShikha, and V. Singh, "Review: Perovskite materials, properties, and their multifunctional applications," *International Journal of Mechanical Engineering*, vol. 7, no. 7, 2022.

[9] H. Zhu, S. Teale, M. N. Lintangpradipto, S. Mahesh, B. Chen, M. D. McGehee, E. H. Sargent, and O. M. Bakr, "Long-term operating stability in perovskite photovoltaics," *Nature Reviews Materials*, vol. 8, no. 9, pp. 569–586, 2023.

[10] W. Li, W. Zhang, S. Van Reenen, R. J. Sutton, J. Fan, A. A. Haghighirad, M. B. Johnston, L. Wang, and H. J. Snaith, "Enhanced uv-light stability of planar heterojunction perovskite solar cells with caesium bromide interface modification," *Energy & Environmental Science*, vol. 9, pp. 490–498, 2016.

[11] X. Du, J. Li, G. Niu, J.-H. Yuan, K.-H. Xue, M. Xia, W. Pan, X. Yang, B. Zhu, and J. Tang, "Lead halide perovskite for efficient optoacoustic conversion and application toward high-resolution ultrasound imaging," *Nature communications*, vol. 12, no. 1, p. 3348, 2021.

[12] A. Mutalikdesai and S. K. Ramasesha, "Emerging solar technologies: Perovskite solar cell," *Resonance*, vol. 22, no. 11, pp. 1061–1076, 2017.

[13] S. D. Stranks, G. E. Eperon, G. Grancini, C. Menelaou, M. J. Alcocer, T. Leijtens, L. M. Herz, A. Petrozza, and H. J. Snaith, "Electron-hole diffusion lengths exceeding 1 micrometer in an organometal trihalide perovskite absorber," *Science*, vol. 342, no. 6156, pp. 341–344, 2013.

[14] E. Edri, S. Kirmayer, A. Henning, S. Mukhopadhyay, K. Gartsman, Y. Rosenwaks, G. Hodes, and D. Cahen, "Why lead methylammonium tri-iodide perovskite-based solar cells require a mesoporous electron transporting scaffold (but not necessarily a hole conductor)," *Nano Letters*, vol. 14, no. 2, pp. 1000–1004, 2014.

[15] D. Bryant, N. Aristidou, S. Pont, I. Sanchez-Molina, T. Chotchunangatchaval, S. Wheeler, J. R. Durrant, and S. A. Haque, "Light and oxygen induced degradation limits the operational stability of methylammonium lead triiodide perovskite solar cells," *Energy & Environmental Science*, vol. 9, pp. 1655–1660, 2016.

[16] M. H. Miah, M. B. Rahman, M. Nur-E-Alam, M. A. Islam, M. Shahinuzzaman, M. R. Rahman, M. H. Ullah, and M. U. Khandaker, "Key degradation mechanisms of perovskite solar cells and strategies for enhanced stability: issues and prospects," *RSC Advances*, vol. 15, p. 628, 2025.

[17] J. H. Noh, S. H. Im, J. H. Heo, T. N. Mandal, and S. I. Seok, "Chemical management for colorful, efficient, and stable inorganic–organic hybrid nanostructured solar cells," *Nano Letters*, vol. 13, no. 4, pp. 1764–1769, 2013.

[18] J. M. Frost, K. T. Butler, F. Brivio, C. H. Hendon, M. van Schilfgaarde, and A. Walsh, "Atomistic origins of high-performance in hybrid halide perovskite solar cells," *Nano Letters*, vol. 14, no. 5, pp. 2584–2590, 2014.

[19] M. I. Asghar, J. Zhang, H. Wang, and P. D. Lund, "Device stability of perovskite solar cells–a review," *Renewable and Sustainable Energy Reviews*, vol. 77, pp. 131–146, 2017.

[20] T. Baikie, Y. Fang, J. M. Kadro, M. Schreyer, F. Wei, S. G. Mhaisalkar, M. Grätzel, and T. J. White, "Synthesis and crystal chemistry of the hybrid perovskite (ch3nh3)pbi3 for solid-state sensitized solar cell applications," *Journal of Materials Chemistry A*, vol. 1, no. 18, pp. 5628–5641, 2013.

[21] K. Fu, A. W. Ho-Baillie, H. K. Mulmudi, and P. T. T. Trang, *Perovskite solar cells: technology and practices*. Apple Academic Press, 2019.

[22] B. Aïssa, A. Ali, and F. El-Mellouhi, "Oxide and organic–inorganic halide perovskites with plasmonics for optoelectronic and energy applications: A contributive review," *Catalysts*, vol. 11, no. 9, p. 1057, 2021. [Online]. Available: https://doi.org/10.3390/catal11091057

[23] M. A. Peña and J. L. G. Fierro, "Chemical structures and performance of perovskite oxides," *Chemical Reviews*, vol. 101, no. 7, pp. 1981–2018, 2001. [Online]. Available: https://doi.org/10.1021/cr980129f

[24] A. Žužić, V. Filipan, I. Sutlović, and J. Macan, "Perovskite oxides for energy applications," *Tehnički vjesnik - Technical Gazette*, vol. 29, no. 4, 2022. [Online]. Available: https://doi.org/10.17559/tv-20210716122507

[25] A. Kumar, A. Raj, G. Jain, B. Singh, and M. Kumar, *Computational Investigations of the Impact of 2D Materials on Perovskite Solar Cells*, ser. Springer Tracts in Electrical and Electronics Engineering (STEEE). Springer Nature, 2026, pp. 205–229. [Online]. Available: https://link.springer.com/chapter/10.1007/978-981-95-6521-4_9

[26] X. Li, Y. Li, H. He, H. Wang, J. Chen, X. Gu, Z. Li, J. F. Garcia, W. Dang, and T. Gatti, "Research progress on 2d and 3d mixed-phase perovskite thin films: Fabrication, materials, optimization and characterization," *Sustainable Chemistry for Energy Materials*, vol. 3, p. 100028, 2026. [Online]. Available: https://doi.org/10.1016/j.scenem.2025.100028

[27] National Renewable Energy Laboratory, "Best research cell efficiencies," https://www.nrel.gov/pv/cell-efficiency.html, 2026, accessed: 2026-07-16.

[28] T. M. Koh, K. Thirumal, H. S. Soo, and N. Mathews, "Multidimensional perovskites: a mixed cation approach towards ambient stable and tunable perovskite photovoltaics," *ChemSusChem*, vol. 9, no. 18, pp. 2541–2558, 2016.

[29] T. Oku, "Crystal structures of perovskite halide compounds used for solar cells," *Reviews in Advanced Materials and Science*, vol. 59, no. 1, pp. 264–305, 2020.

[30] T. Dawa and B. Sajjadi, "Exploring the potential of perovskite structures for chemical looping technology: A state-of-the-art review," *Fuel Processing Technology*, vol. 253, p. 108022, 2024. [Online]. Available: https://doi.org/10.1016/j.fuproc.2023.108022

[31] S. G. Cao, Z. E. Bi, T. J. Zheng, S. Z. Luo, L. G. Gutsev, B. R. Ramachandran, V. V. Ozerova, N. A. Emelianov, N. A. Slesarenko, Y. P. Zheng, B. Z. Taye, G. L. Gutsev, S. M. Aldoshin, P. A. Troshin, and X. Q. Xu, "Revealing interaction of fluorinated propylamine hydrochloride with precursor and defect states of perovskite films toward efficient flexible solar cells," *Advanced Functional Materials*, vol. 34, no. 42, p. 2405078, 2024.

[32] S. Panda, S. Barik, R. P. SAHU, A. P. SAHU, S.Mishra, and S. Parida, "Studies of structural, microstructural, dielectric, and electrical characterization of binaznmoo6 double perovskite," *Journal of Metals, Materials and Minerals*, vol. 35, no. 2, p. e2244, 2025.

[33] Y. Tachibana, L. Vayssieres, and J. R. Durrant, "Artificial photosynthesis for solar water-splitting," *Nature Photonics*, vol. 6, no. 8, pp. 511–518, 2012.

[34] J.-M. Lehn and R. Ziessel, "Photochemical generation of carbon monoxide and hydrogen by reduction of carbon dioxide and water under visible light irradiation," *Proceedings of the National Academy of Sciences*, vol. 79, no. 2, pp. 701–704, 1982.

[35] Y. Wu, P. Wang, X. Zhu, Q. Zhang, Z. Wang, Y. Liu, G. Zou, Y. Dai, M. H. Whangbo, and B. Huang, "Composite of ch3nh3pbi3 with reduced graphene oxide as a highly efficient and stable visible-light photocatalyst for hydrogen evolution in aqueous hi solution," *Advanced Materials*, vol. 30, no. 10, p. 1704342, 2018.

[36] C. Li, X. Lu, W. Ding, L. Feng, Y. Gao, and Z. Guo, "Formability of ABX_3 ($X = F, Cl, Br, I$) halide perovskites," *Acta Crystallographica Section B*, vol. 64, no. 6, pp. 702–707, 2008.

[37] C. J. Bartel, C. Sutton, B. R. Goldsmith, R. Olasagasti, C. B. Musgrave, and A. M. Holder, "New tolerance factor to predict the stability of perovskite oxides and halides," *Science Advances*, vol. 5, no. 2, p. eaav0693, 2019.

[38] J. Kangsabanik, V. Sugathan, A. Yadav, A. Yella, and A. Alam, "Double perovskites overtaking the single perovskites: A set of new solar harvesting materials with much higher stability and efficiency," *Physical Review Materials*, vol. 2, p. 055401, 5 2018. [Online]. Available: https://link.aps.org/doi/10.1103/PhysRevMaterials.2.055401

[39] A. Jain, O. Voznyy, and E. H. Sargent, "High-throughput screening of lead-free perovskite-like materials for optoelectronic applications," *The Journal of Physical Chemistry C*, vol. 121, no. 13, pp. 7183–7187, 2017. [Online]. Available: https://doi.org/10.1021/acs.jpcc.7b02221

[40] L. Chu, W. Ahmad, W. Liu, J. Yang, R. Zhang, Y. Sun, J. Yang, and X. Li, "Lead-free halide double perovskite materials: A new superstar toward green and stable optoelectronic applications," *Nano-Micro Lett.*, vol. 11, p. 16, 2019.

[41] T. Islam *et al.*, "Simulation studies to quantify the impacts of point defects: An investigation of $cs_2agbibr_6$ perovskite solar devices utilizing zno and cu_2o as the charge transport layers," *Computational Materials Science*, vol. 184, p. 109865, 2020. [Online]. Available: https://doi.org/10.1016/j.commatsci.2020.109865

[42] Z. Hasan, M. A. Rahman, D. K. Das, and H. K. Rouf, "Influence of ca doping in structural, electronic, optical and mechanical properties of ba1- xcaxtio3 perovskite from first-principles investigation," *Scientific Reports*, vol. 13, no. 1, p. 10487, 2023.

[43] H.-J. Sung, Y. Mochizuki, and F. Oba, "Surface reconstruction and band alignment of non-metallic a (ii) b (iv) o 3 perovskites," *Physical Review Materials*, vol. 4, no. 4, p. 044606, 2020.

[44] M. Loletti, C. Borghesi, R. Rurali, and G. Giorgi, "Structural and electronic properties of catio3 polymorphs and 2d-derived systems: a theoretical investigation," *The European Physical Journal B*, vol. 98, no. 4, p. 77, 2025.

[45] C. Berglund and W. Baer, "Electron transport in single-domain, ferroelectric barium titanate," *Physical Review*, vol. 157, no. 2, p. 358, 1967.

[46] M. A. Karim, A. Saha, M. J. Hossain, M. S. Kabir, M. O. Faruk, M. A. Khatun, M. R. Khan, and D. C. Roy, "Role of oxygen vacancies on the structural, electronic, optical, and photocatalytic properties of ba2cemo6 (m= bi, sb) double perovskites: a dft study," *Scientific Reports*, vol. 16, no. 1, p. 11973, 2026.

[47] J. Gao, W. Zeng, B. Tang, M. Zhong, and Q.-J. Liu, "Optical, electronic, and mechanical properties of p-type conductive oxide babio3: A density functional theory study," *Chemical Physics Letters*, vol. 761, p. 138054, 2020.

[48] R. Martoňák, D. Ceresoli, T. Kagayama, Y. Matsuda, Y. Yamada, and E. Tosatti, "High-pressure phase diagram, structural transitions, and persistent nonmetallicity of babio 3: Theory and experiment," *Physical Review Materials*, vol. 1, no. 2, p. 023601, 2017.

[49] A. S. Chouhan, E. Athresh, R. Ranjan, S. Raghavan, and S. Avasthi, "Babio3: A potential absorber for all-oxide photovoltaics," *Materials Letters*, vol. 210, pp. 218–222, 2018.

[50] D. Abdullah and D. C. Gupta, "A dft investigation of lead-free rb2ycux6 (x= cl, br, i) perovskites for potential applications in solar cells and thermoelectric devices," *Optical and Quantum Electronics*, vol. 56, no. 11, p. 1846, 2024.

[51] I. A. Apon, K. Kriaa, M. A. Rahman, M. Alamgir Hossain, C. Maatki, A. A. Assadi, and N. Elboughdiri, "Rb2bx6 double perovskites: unlocking 22% efficiency through structural, electronic, mechanical, and optical insights," *RSC advances*, vol. 15, no. 47, pp. 40 209–40 230, 2025.

[52] R. C. MacKenzie, T. Kirchartz, G. F. Dibb, and J. Nelson, "Modeling nongeminate recombination in p3ht: Pcbm solar cells," *The Journal of Physical Chemistry C*, vol. 115, no. 19, pp. 9806–9813, 2011.

[53] R. Hanfland, M. A. Fischer, W. Brütting, U. Würfel, and R. C. MacKenzie, "The physical meaning of charge extraction by linearly increasing voltage transients from organic solar cells," *Applied Physics Letters*, vol. 103, no. 6, 2013.

[54] R. C. MacKenzie, C. G. Shuttle, M. L. Chabinyc, and J. Nelson, "Extracting microscopic device parameters from transient photocurrent measurements of p3ht: Pcbm solar cells," *Advanced Energy Materials*, vol. 2, no. 6, pp. 662–669, 2012.

[55] T. Goudon, V. Miljanović, and C. Schmeiser, "On the shockley–read–hall model: generation-recombination in semiconductors," *SIAM Journal on Applied Mathematics*, vol. 67, no. 4, pp. 1183–1201, 2007.

[56] D. A. Noori, "Heterojunction active layer mapbi3/cspbi3 design for high-performance perovskite solar cells: a computational analysis achieving 20.5% efficiency," *Journal of Computational Electronics*, vol. 24, no. 2, p. 43, 2025.

[57] M. Kibbou, Z. Haman, I. Bouziani, N. Khossossi, Y. Benhouria, I. Essaoudi, and R. Ahuja, "Cs2ingax6 (x = cl, br, or i): emergent inorganic halide double perovskites with enhanced optoelectronic characteristics," *Current Applied Physics*, vol. 21, pp. 50–57, 2021.

[58] M. A. Karim, A. Saha, M. J. Hossain, M. S. Kabir, M. O. Faruk, M. A. Khatun, M. R. Khan, and D. C. Roy, "Role of oxygen vacancies on the structural, electronic, optical, and photocatalytic properties of ba2cemo6 (m = bi, sb) double perovskites: a dft study," *Scientific Reports*, vol. 16, no. 1, p. 39601, 2026.

Supplementary Files

This is a list of supplementary files associated with this preprint. Click to download.

- Alldatas.rar